

# A power-law description of heavy ion collision centrality

Thomas A. Trainor and Duncan J. Prindle  
*CENPA, Box 354290, University of Washington, Seattle, WA 98195*  
(Dated: December 2, 2024)

The minimum-bias distribution on heavy ion collision multiplicity  $n_{ch}$  is well approximated by power-law form  $n_{ch}^{-3/4}$ , suggesting that a change of variable to  $n_{ch}^{1/4}$  may provide more precise access to the structure of the distribution and to A-A collision centrality. We report here a detailed centrality study of *Hijing-1.37* Monte Carlo data at 200 GeV using the power-law format. We also find that the minimum-bias distribution on  $n_{part}^{1/4}$ , determined with a Glauber Monte Carlo simulation, is uniform except for a 5% sinusoidal variation. The power-law format reveals precise linear relations between Glauber parameters  $n_{part}$  and  $n_{bin}$  and the fractional cross section. The power-law format also facilitates incorporation of extrapolation constraints on data and Glauber distributions to improve the centrality accuracy for peripheral collisions by more than 10×.

PACS numbers: 24.60.Ky,25.75.Gz

Keywords: Collision centrality, heavy ion collisions, participant scaling, binary-collision scaling, Glauber model, two-component model, *Hijing* simulation

## I. INTRODUCTION

Recent observations of fluctuations and correlations in RHIC Au-Au collisions [1, 2, 3] reveal *rapid changes* of correlation structure with heavy ion collision centrality, and in some cases a trend to nearly linear dependence on mean participant path length. The mechanisms for at least some of those changes seem to be related to recently-observed copious low- $Q^2$  parton scattering as a factor in bulk-medium formation and dynamics [4]. Correlation measurements for p-p collisions [5] provide a precision reference for peripheral Au-Au collisions. The centrality dependence of the newly-observed correlation phenomena, as well as global quantities such as  $n_{ch}$  and  $\langle p_t \rangle$ , now require substantially more accurate determination of collision centrality than has been achieved previously.

It has been observed that the minimum-bias distribution on multiplicity in heavy ion collisions is well approximated by a *power-law distribution* [6], implying that a change of variable could provide a simpler and more precise characterization of the distribution. The resulting power-law form of the minimum-bias distribution is revealed as a *precision reference*, relative to which small differences in *measured* minimum-bias distributions are more easily identified and studied.

Heavy ion centrality has three aspects: 1) determine the relation between an observable such as particle multiplicity and a collision geometry parameter such as impact parameter or participant number, 2) determine the centrality dependence of particle and transverse-momentum production and other physical processes, and 3) measure the differential and total cross sections for a given collision system. The main subject of this paper is 1) centrality determination in a power-law context. We also consider examples of 2) particle,  $p_t$  and  $E_t$  production, using the *Hijing* Monte Carlo and RHIC data to illustrate applications of the power-law method.

In this paper we introduce the power-law form of the minimum-bias distribution on event multiplicity  $n_{ch}$  and

use it to study the relation of multiplicity to fraction of total cross section, participant number and participant mean path length. We show that the shape of the data distribution is a consequence of the nearly-exact power-law form of the minimum-bias distribution on participant number  $n_{part}$ , as obtained from a Monte Carlo Glauber simulation. As a demonstration of the method we obtain the detailed dependence on collision centrality of particle and  $p_t$  production in *Hijing-1.37*-simulated collisions for two event classes and particle and  $E_t$  production in RHIC data. We employ the simple structure of the power-law format to refine the problem of centrality definition and substantially reduce systematic error.

We first describe *Hijing-1.37* simulations for two event classes, then compare the conventional and power-law forms of the minimum-bias distribution for *Hijing* and RHIC data. We study the Glauber model in two versions and obtain precise algebraic representation of its output parameters in terms of the fractional cross section. We then describe the process of centrality determination for conventional and power-law methods and compare systematic errors and uncertainties for the two methods. Finally, we determine the centrality dependence of particle number,  $p_t$  and  $E_t$  in the power-law context.

## II. HIJING DATA

We used Monte Carlo event generator *Hijing-1.37* [7] to produce minimum-bias event ensembles with  $\sim 1M$  total events for each of two conditions: 1) *quench-off* *Hijing* – jet production enabled but no jet quenching and 2) *default* or *quench-on* *Hijing* – jet production and jet quenching enabled. Jet quenching in *Hijing* simulates the dissipative effect of the QCD medium on energetic partons, modeling parton energy loss (*via* pQCD bremsstrahlung) and its consequences for particle production. Charged particles with pseudorapidity  $|\eta| < 1$ , transverse momentum  $p_t \in [0.15, 2]$  GeV/c and full azimuth were accepted.

The total charged-particle multiplicity in the acceptance for each event defines quantity  $n_{ch}$ .

The two event classes, quench-on and quench-off, can be distinguished to an extent *depending on the analysis method*. Whatever the physical validity of *Hijing* and its pQCD jet quenching mechanism, the two event classes provide a means to assess in this study the sensitivity of different centrality presentation formats to physical models. At each stage of centrality determination we compare the two event types to assess sensitivity to collision dynamics and mechanisms of particle and  $p_t$  production.

### III. CONVENTIONAL MINIMUM-BIAS DISTRIBUTION

In Fig. 1 (left panel) the minimum-bias distribution of event number on particle multiplicity  $n_{ch}$  is plotted in a conventional semi-log plotting format for *Hijing* quench-off and default events. The semi-log plots appear to be monotonically decreasing, and the tails at large  $n_{ch}$  reflect fluctuations in particle production for central collisions (maximum participant number, impact parameter  $b = 0$ ). The relative magnitude of fluctuations depends on detector acceptance and tracking efficiency. Comparing the distributions for quench-on and quench-off *Hijing* in this format, the only apparent difference is in the endpoint positions. There is otherwise no visible difference between the two event types.

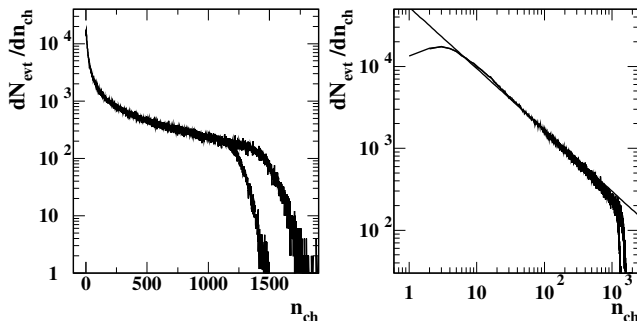


FIG. 1: Left panel: Minimum-bias distributions for quench-off and quench-on (larger endpoint) *Hijing* collisions plotted with a conventional semi-log plotting format. Right panel: The same distributions plotted with a log-log format. The line represents an  $n_{ch}^{-3/4}$  power-law trend.

In Fig. 1 (right panel) the same distributions, plotted in a log-log format, reveal an interesting feature: the distributions are well approximated by power-law trend  $n_{ch}^{-3/4}$  (solid line) [6]. That trend suggests that a change of variable might provide more precise access to distribution structure. Interpreting  $n_{ch}^{-3/4}$  as the Jacobian of a variable transformation we observe that if  $d\sigma/dn_{ch} \propto n_{ch}^{-3/4}$  then  $n_{ch}^{3/4} d\sigma/dn_{ch} \sim \text{constant}$ . But  $dn_{ch} = 4n_{ch}^{3/4} dn_{ch}^{1/4}$ , so  $d\sigma/dn_{ch}^{1/4} \sim \text{constant}$ . We therefore convert the minimum-bias distributions for *Hijing*

data to *power-law* form  $d\sigma/dn_{ch}^{1/4} \equiv 4n_{ch}^{3/4} d\sigma/dn_{ch}$  to provide more precise access to data and possibly improved determination of collision centrality.

### IV. POWER-LAW MINIMUM-BIAS DISTRIBUTION

Fig. 2 (left panel) shows unit-normal plots of  $d\sigma/dn_{ch}^{1/4}$  vs  $n_{ch}^{1/4}$  which confirm the basic features anticipated for the power-law plotting format—an approximately rectangular distribution with limited amplitude variation and well-defined endpoints. The distribution has been re-binned into 50 uniform bins on  $n_{ch}^{1/4}$  (App. A 3), insuring nearly-uniform statistical error while retaining adequate resolution for significant structure. The points indicate the edge resolution with this binning scheme. The first few points are defined by the lowest integers, not the uniform binning.

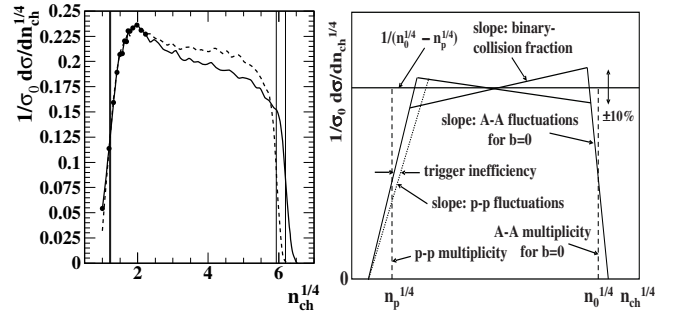


FIG. 2: Left panel: The power-law form of minimum-bias distribution for quench-on (solid curve) and quench-off (dashed curve) *Hijing* data. Left and right vertical lines indicate positions of endpoint  $n_p^{1/4}$  for both event types and  $n_0^{1/4}$  for quench-off and quench-on collisions. Right panel: A cartoon of the power-law minimum-bias distribution identifying principal features.

Five parameters describe the power-law distribution, as summarized in Fig. 2 (right panel): 1) The upper half-maximum point  $n_0$  estimates the mean  $n_{ch}$  corresponding to central collisions ( $b = 0$ ) and endpoint  $n_{part,max}$  of the minimum-bias distribution on participant number  $n_{part}$ . 2) The lower half-maximum point  $n_p$  estimates the mean  $n_{ch}$  for p-p collisions ( $n_{part} = 2$ ). 3,4) The slopes at the endpoints measure *relative* particle-production fluctuations in p-p and central ( $b = 0$ ) A-A collisions, which also depend on the detector acceptance. *Relative* fluctuations are larger for smaller acceptance:  $\sigma_{n_{ch}}/\bar{n}_{ch} \propto 1/\sqrt{n_{ch}} \propto 1/\sqrt{\text{acceptance}}$ . 5) The slope of the distribution near the midpoint is related to the fraction of produced particles which scale with the number of binary nucleon-nucleon collisions (binary-collision scaling, hard processes). Those five features adequately represent the shape of the minimum-bias distribution with respect to collision centrality and particle production. Smaller features are strongly suppressed by the running integration

used to relate  $n_{ch}$  to centrality. Additional variation of data near  $n_p$  may represent trigger and/or vertex inefficiencies, typically largest for small values of  $n_{ch}$ . In Fig. 2 (left panel)  $n_p = 2.3$  and  $n_0 = 1235$  (1465) for quench-off (quench-on) events respectively.

In this unit-normal power-law format quench-on and quench-off trends are now clearly and precisely differentiated, revealing physics-related differences at the few-percent level not accessible in the semi-log plotting format of Fig. 1. The shape of the distribution at upper endpoint  $n_0$  makes  $b = 0$  parameters precisely accessible. It is notable that the distributions for two event classes coincide for peripheral collisions below  $n_{ch}^{1/4} \sim 2.5$ , confirming that, for this Monte Carlo at least, the minimum-bias distribution is asymptotically independent of the complex dynamics of heavy ion collisions, is determined solely by a linear superposition of N-N collisions in that region. We will return to that issue when considering application of *extrapolation constraints* to reduce systematic error. To insure that this power-law trend is not unique to the *Hijing* Monte Carlo we consider in the power-law context the structure of a minimum-bias distribution obtained from RHIC data.

## V. RHIC DATA

Fig. 3 shows a measured minimum-bias distribution on  $n_{h-}$  (negative hadron yield) into one unit of pseudorapidity for 60k Au-Au collisions at  $\sqrt{s_{NN}} = 130$  GeV [10]. The analysis of that distribution illustrates several aspects of the collision geometry problem for real data. The left panel shows the conventional semi-log plotting format uniformly binned on  $n_{h-}$ . The total cross section was assumed to be  $\sigma_{tot} = 7.2$  barns [8]. The trigger efficiency (coincidence of two ZDCs [10]) was at least 99% for all multiplicities. The measured vertex efficiency was 100% for  $n_{h-} > 50$  but dropped to 60% below  $n_{h-} = 5$ . The contribution to  $\sigma_{tot}$  from the lowest bin was estimated to be 21% based on an extrapolation using *Hijing*. It was argued that peripheral nucleus-nucleus collisions are linear in N-N collisions, and that *Hijing* models N-N collisions well. *Hijing* was normalized to data in the  $n_{h-}$  interval [5,25] ([1.5,2.65] on  $n_{h-}^{1/4}$ ) and used for the extrapolation below  $n_{h-} = 5$ . The overall systematic uncertainty in the inferred differential cross section was stated to be 10%, due to uncertainties in  $\sigma_{tot}$  and the inferred relative contribution from the first bin based on the *Hijing* extrapolation.

Fig. 3 (right panel) shows the same data plotted in the power-law format (including the first bin of the analysis, bounded above by the dash-dot line at  $n_{h-} = 5$ ). This result confirms that the power-law format is also relevant to RHIC data. Quantitative details of the distribution are revealed in this linear plot which are not accessible in the conventional semi-log format. Of the five parameters representing the power-law distribution two can be obtained from these data: the upper endpoint

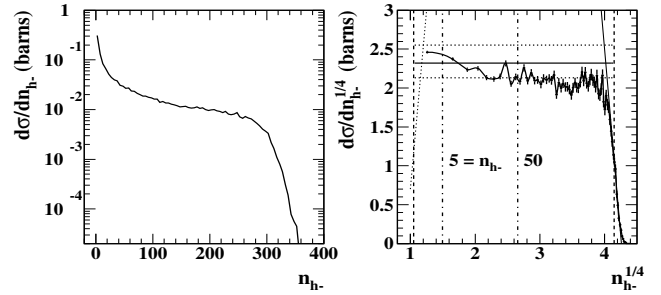


FIG. 3: Left panel: A minimum-bias distribution of RHIC data [10] with a conventional semi-log plotting format. Right panel: The same data plotted with a power-law format.

$n_0$  and the fluctuation width (slope) at  $n_0$ . We obtain  $n_0 \sim 4.15^{1/4} = 297$  (mean  $n_{h-}$  for  $b = 0$ ). The slope at the midpoint is questionable due to corrections based on the *Hijing* extrapolation (discussed further below). Endpoint  $n_p$  and the fluctuation slope at  $n_p$  are obviously inaccessible due to efficiency and background uncertainties and the binning scheme. The left edge can be sketched (thin dotted line) based on the expected p-p  $h^-$  yield  $n_p^{1/4} = 1.12^{1/4} = 1.03$  (corrected  $n_{p-p} = n_{ph+} + n_{ph-}$  should be about 2.25 in one unit of rapidity [14]).

The horizontal solid line in the right panel represents the *power-law reference* corresponding to the assumed  $\sigma_{tot} = 7.2$  barns distributed uniformly on the interval between the estimated  $n_p^{1/4}$  and the observed  $n_0^{1/4}$ . The dotted lines represent the stated 10% systematic uncertainty. The data fall substantially below the solid line over most of the observed distribution. The systematic offset may be due to the assumption that the left-most bin is 21% of  $\sigma_{tot}$  based on the *Hijing* extrapolation. That bin actually represents at most 15% of  $\sigma_{tot}$  based on its width. The fraction may be less, given the expected fall-off near  $n_p$ . The lowest-bin fraction was thus possibly overestimated by 6-10%, which would account for the underestimate of the average differential cross section in the region above  $n_{h-} = 5$  visible in Fig. 3 (right panel). The shape of this data distribution in the region of more-central collisions ( $n_{h-}^{1/4} > 2.5$ ) strongly disagrees with default *Hijing* in Fig. 2 (left panel).

This example from RHIC data illustrates how a minimum-bias distribution is conventionally calibrated to obtain a differential cross-section distribution, and what information is accessible from the two plotting formats. When plotted with the semi-log format, *Hijing* and data appear equivalent, as stated in [10]. However, the physical information in the distribution lies typically within a 20% vertical band accessible only when plotted with a linear power-law format, not on a logarithmic scale covering four or five decades. The power-law format reveals details of the distribution relevant to collision geometry and to particle production, permitting detailed comparison of models to data and inspection of data for systematic errors. The next step in centrality determination

is to integrate the corrected minimum-bias distribution to obtain the relation between  $n_{ch}$  and fractional cross section  $\sigma/\sigma_{tot}$ . First, we examine Glauber-model simulations of heavy ion collisions in a power-law context.

## VI. THE GLAUBER MODEL

The Glauber model of nucleus-nucleus collisions invokes an eikonal approximation to represent many nucleon-nucleon interactions within the two-nucleus overlap region in a calculable form. The nuclear-matter distribution is modeled by a Woods-Saxon (W-S) function with parameters derived from electron scattering. The nucleon distribution is modeled either as a continuum W-S distribution (optical Glauber) or as a random nucleon distribution relative to the W-S density (Monte Carlo Glauber). In either case, the quantities of interest are participant number  $n_{part}$ , binary-collision number  $n_{bin}$ , mean nucleon path length  $\nu \approx 2 n_{bin}/n_{part}$  and cross section  $\sigma$  in relation to impact parameter  $b$ . Precise determination of  $n_{part}$ ,  $n_{bin}$  and  $\nu$  (estimating mean participant path length in number of *encountered* nucleons) in relation to fractional cross section  $\sigma(b)/\sigma_{tot}$  is required to establish the centrality dependence of particle production and correlations. The optical and Monte Carlo procedures as described below are derived in part from [11, 12].

### A. Optical Glauber

The optical Glauber uses an analytic approach to relate various quantities to  $b$  through integrals of the nuclear density. The basic model is normalized probability density  $\rho_A(\vec{r})$ , a 3D nuclear density with a Woods-Saxon radial form. The projection onto a plane normal to collision axis  $z$  (single-particle areal density) for nucleus  $A$  is defined by  $T_A(\vec{s}) \equiv \int dz \rho_A(\vec{s}, z)$ . The *overlap integral* (two-particle areal density) for nuclei  $A$  and  $B$  is then defined by  $T_{AB}(b) \equiv \int d\vec{s} T_A(\vec{s}) T_B(\vec{s} - \vec{b})$ , an auto-correlation distribution for  $T_A(\vec{s})$  if  $A = B$ .  $n_{part}(b)$ ,  $n_{bin}(b)$  and  $d\sigma(b)/d\pi b^2$  are defined as integrals of  $T_A$  combined with the appropriate nucleon-nucleon cross section  $\sigma_{NN}$  [11].  $n_{bin}(b) \equiv \int d\vec{s} AT_A(\vec{s}) \sigma_{NN} BT_B(\vec{s} - \vec{b})$  and for  $A, B \gg 1$ ,  $d\sigma(b)/d\pi b^2 \simeq 1 - \exp\{-n_{bin}(b)\}$  and  $n_{part}(b)/2 \simeq \int d\vec{s} AT_A(\vec{s}) \{1 - \exp[-\sigma_{NN} BT_B(\vec{s} - \vec{b})]\}$ . The optical Glauber total cross section for Au-Au at 130 GeV was determined to be  $\sigma_{tot} \equiv \pi b_0^2 = 7.05$  barns in [11]. The expression for  $d\sigma(b)/d\pi b^2$  implies that  $n_{bin}(b_0) \sim \ln(2) < 1$  (and in fact goes asymptotically to zero for large  $b$ ), whereas we expect  $n_{bin}$  for real nuclei to go asymptotically to 1 *from above* for peripheral collisions. Given its optical Glauber definition,  $n_{part}/2 \rightarrow n_{bin}$  for large  $b$  and the same problem arises.

### B. Monte Carlo Glauber

The Monte Carlo Glauber simulates an ensemble of A-B collisions corresponding to a distribution of samples on impact parameter  $b$  (samples uniform on  $b^2$ ). Each collision combines two random nucleon distributions sampled from Woods-Saxon nuclear density  $\rho_A(\vec{r})$ . From the event ensemble one can construct distributions of  $n_{part}(b)$  and  $n_{bin}(b)$  as correlated random variables. One also obtains differential cross-section distributions on  $n_{part}$  and  $n_{bin}$  important for the power-law method described below. The Monte Carlo Glauber total cross section for Au-Au at 130 GeV was determined to be  $\sigma_{tot} = 6.8$  barns in [11], compared to 6.9 barns quoted in [10, 12], 7.05 barns from the optical Glauber quoted above and 7.2 barns in [8].

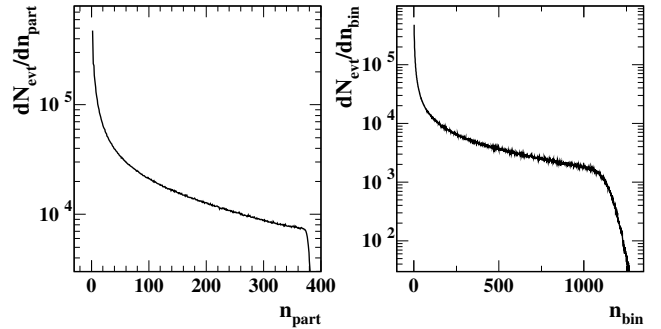


FIG. 4: Left panel: The conventional minimum-bias distribution on participant number obtained from a Monte Carlo Glauber simulation [9]. Right panel: The corresponding distribution on binary-collision number.

Fig. 4 shows minimum-bias distributions from a Monte Carlo Glauber simulation for 200 GeV Au-Au collisions [9] plotted in the conventional semi-log format. When plotted in log-log format we observe that the distribution on  $n_{part}$  precisely follows the power-law trend  $n_{part}^{-3/4}$  similar to data, whereas the distribution on  $n_{bin}$  follows the power-law trend  $n_{bin}^{-5/6}$ . Those trends suggest transformations to distributions on  $n_{part}^{1/4}$  and  $n_{bin}^{1/6}$ .

### C. Power-law Glauber

We apply the power-law approach to Monte Carlo Glauber parameters  $n_{bin}$  and  $n_{part}$ , transforming the distributions in Fig. 4 as noted. In Fig. 5 (left panels) we plot power-law minimum-bias distributions on  $(n_{part}/2)^{1/4}$  and  $n_{bin}^{1/6}$  from the Monte Carlo Glauber. On the right end the distributions are bounded (half-maximum points) by  $(n_{part,max}/2)^{1/4} = 3.72$  and by  $n_{bin,max}^{1/6} = 3.23$ . The corresponding limiting values are  $n_{part,max}/2 = 191$  and  $n_{bin,max} = 1136$ . The distributions are nearly rectangular, as expected, and the distribution on  $(n_{part}/2)^{1/4}$  is especially simple, being a con-

stant plus a sinusoid with 5% relative amplitude (modeled by the dashed curve just visible at the left end of the upper-left plot). Note the sensitivity of the power-law format to meaningful detail; such precise details, at the 1% level, are completely inaccessible in the semi-log format of Fig. 4 (left panel). The distributions are normalized in these plots (W) to obtain unit mean amplitude. We find that the observed *approximate* power-law trend for the minimum-bias distribution on  $n_{ch}$  is a consequence of the nearly-exact power-law trend on  $n_{part}$ . Whatever its origins, we capitalize on the simplicity of that trend to refine the problem of centrality definition and particle and  $p_t$  production.

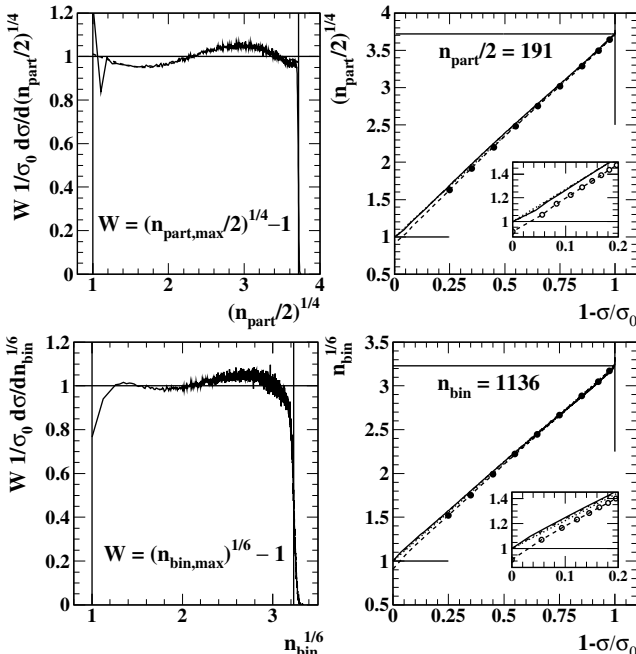


FIG. 5: Left panels: Power-law minimum-bias distributions on participant-pair (upper) and binary-collision (lower) numbers, obtained from a Glauber Monte Carlo simulation [9]. The upper half-maximum values are 3.72 and 3.23 respectively. Right panels: The solid curves are running integrals of the distributions in the left panels. The dotted lines are power-law references. The solid points represent a Monte-Carlo Glauber simulation with binned centrality [12]. The dashed curves represent an alternative integral definition.

Fig. 5 (right panels) shows the relations which connect  $n_{part}/2$  and  $n_{bin}$  to centrality measured by fractional cross section  $1 - \sigma/\sigma_0$ . The solid curves are *running integrals* of the distributions in the left panels (App. A 4). The other curves and points are described below. The power-law format provides a simple means to parameterize those relations precisely. For the purpose of centrality determination the power-law Glauber curves at 200 GeV are well represented by linear expressions  $(n_{part}/2)^{1/4} = 1 + 2.72(1 - \sigma/\sigma_0)$  and  $n_{bin}^{1/6} = 1 + 2.23(1 - \sigma/\sigma_0)$ . For studies of *particle production* the 5% sinusoid should be included in the

$(n_{part}/2)^{1/4}$  parameterization, as discussed further in Sec. X. The Monte Carlo Glauber results are thus represented precisely (< 2%) by four numbers: exponents  $1/4$  and  $1/6$  and upper limits  $n_{part,max}$  and  $n_{bin,max}$ . The simple linear parameterizations, the ability to make precise visual comparisons and specific expectations for limiting cases (extrapolation constraints) illustrate the value of the power-law format for the Glauber model.

Also plotted in Fig. 5 (right panels) are data (nine solid points) from an independent Monte Carlo Glauber simulation based on binning the fractional cross section [12]. For both  $(n_{part}/2)^{1/4}$  and  $n_{bin}^{1/6}$  the results agree for the most central collisions (at right) but significantly disagree for more-peripheral collisions, and extrapolate to the wrong limiting values for peripheral collisions ( $\neq 1$ ). Those deviations are discussed in App. A 5 and may result from different definitions of the running integrals. The insets provide detailed views of the peripheral region. The dashed curves (which pass precisely through the solid data points) and open circles (one for each entry in the minimum-bias histogram) correspond to one integral definition (alternative), the solid curves to another (recommended). The dashed curves go asymptotically to effective bin edges  $0.7^{1/4} = 0.915$  on  $(n_{part}/2)^{1/4}$  and  $0.6^{1/6} = 0.918$  on  $n_{bin}^{1/6}$  (App. A 5). The dotted lines in all cases represent the power-law reference.

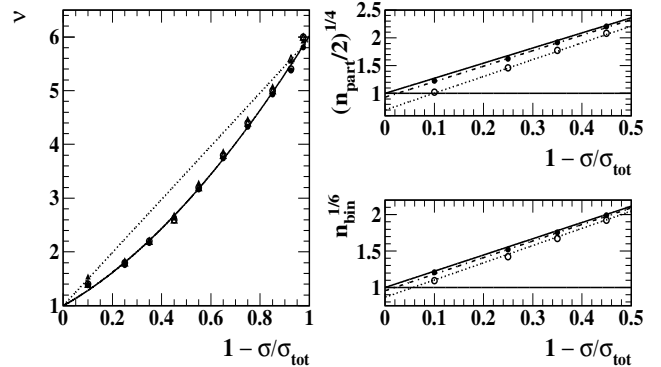


FIG. 6: Left panel: Participant mean path length  $\nu$  vs fractional cross section. The solid curve is derived from running integrals in Fig. 5 (right panels). The points represent several binned Glauber results [12]. Right panels: Detailed views of Glauber power-law trends showing deviations. The solid lines are derived from the running integrals in Fig. 5 (right panels). The points are from two Glauber simulations [12]. The dotted and dash-dot lines extrapolate the points.

With expressions for  $(n_{part}/2)^{1/4}$  and  $n_{bin}^{1/6}$  vs fractional cross section established we now define participant path-length estimator  $\nu$ . The pathlength concept originated with h-A experiments [13] in which  $\nu$  was defined in terms of a hadron interaction length in nucleus A, depending on the hadron-nucleon center-of-mass energy. We prefer a purely geometric path-length estimator defined in terms of *encountered nucleons* rather than a specific nuclear interaction, with limiting value 1 for peripheral A-A. The

starting point is conventional Monte Carlo Glauber parameters:  $\nu = 2n_{bin}/n_{part}$ . Using the parametric expressions above we have

$$\nu = \{1 + 2.23(1 - \sigma/\sigma_0)\}^6 / \{1 + 2.72(1 - \sigma/\sigma_0)\}^4. \quad (1)$$

Fig. 6 (left panel) shows  $\nu(\sigma/\sigma_0)$  from Eq. (1) as the solid curve with maximum value near 6. The dotted line  $1 + 5(1 - \sigma/\sigma_{tot})$  provides a curvature reference. This result corresponds to  $\sigma_{NN}$  for 200 GeV N-N collisions ( $n_{bin} \propto \sigma_{NN}$  for central collisions).

Fig. 6 (right panels) compares results from optical, Monte Carlo and power-law Glaubers. Only the lower half of the centrality range is shown to improve sensitivity. The solid curves are the parameterizations derived from the running integrals of minimum-bias distributions shown in Fig. 5 (right panels). The open circles and solid points are centrality-bin mean values from the optical and Monte Carlo Glauber results respectively in Tables II and III of [12]. The dash-dot and dotted lines in the upper-right panel represent 2.5% and 10% offsets respectively on  $1 - \sigma/\sigma_{tot}$  at the peripheral end (compared at the horizontal reference line). A 2.5% relative error in  $\sigma/\sigma_{tot}$  for peripheral collisions propagates to a  $\sim 30\%$  error in  $n_{part}$  (see Sec. IX B on Glauber errors). That large systematic error has negative implications for per-participant particle production measurements.

#### D. Bin averages

The points in the left panel of Fig. 6 compare averages  $\nu = 2\langle n_{part} \rangle / \langle n_{part} \rangle$  and  $\nu = 2\langle n_{bin} / n_{part} \rangle$  for optical and Monte Carlo Glaubers (four sets of points) with the power-law analytic expression for  $\nu$ . The coincidence is notable in view of the significant discrepancies in  $n_{part}$  and  $n_{bin}$  in the right panels. The solid curve from the power-law parameterization also corresponds to  $\nu = 2\langle n_{bin}^{1/6} \rangle^6 / \langle n_{part}^{1/4} \rangle^4$ , since those quantities are nearly linearly related to the fractional cross section. From this comparison we conclude that  $\nu$  provides excellent *common-mode reduction* of total cross-section and other Glauber systematic errors.

A possible source of the discrepancy between Monte Carlo (solid points) and running-integral (solid lines) Glauber results in Fig. 6 (right panels) is the difference between mean values of powers and powers of mean values. However, that difference actually works in the wrong direction. The bin mean  $\langle n_{part} \rangle$  from the Monte Carlo Glauber (effectively  $\langle (n_{part}^{1/4})^4 \rangle$ —the mean of a power) should be *larger* than the corresponding running-integral value ( $\langle n_{part}^{1/4} \rangle^4$ —the power of a mean). The maximum difference  $\langle n_{part} \rangle^{1/4} - \langle n_{part}^{1/4} \rangle$  (for peripheral collisions), determined with the power-law parameterization, is in fact positive but small, less than 0.7% for 10%-wide centrality bins, and less than 0.2% for 5%-wide centrality bins. We conclude that the order of averaging is of no

consequence at the 1% level of precision. The corresponding differences in Fig. 6 (right panels) are negative, and so must have a different cause. For the Monte Carlo Glauber the differences apparently arise from the integral definition (App. A 5).

## VII. CONVENTIONAL CENTRALITY

Having described several approaches to Glauber modeling of collision centrality we now return to the collision-geometry problem in the data context. Trigger inefficiency (typically a small effect for all  $n_{ch}$ ) and vertex-finding inefficiency (possibly large for small  $n_{ch}$ ) require corrections. In a conventional centrality determination the raw minimum-bias distribution  $dN_{evt}/dn_{ch}$  is corrected for event-trigger, vertex-reconstruction and particle-detection inefficiencies and backgrounds (*e.g.*, beam-gas collisions and photonuclear excitations). Collision events lost by mechanisms depending on event multiplicity  $n_{ch}$  distort the minimum-bias distribution and contribute systematic error to centrality determination. Particle detection inefficiencies systematically shift events to lower  $n_{ch}$ . The corrected, normalized distribution  $d\sigma(n_{ch})/dn_{ch}$  should integrate to the physical total cross section  $\sigma_{tot}$  corresponding to the ideal trigger definition.

The correspondence between the minimum-bias data distribution and Glauber-model geometry parameters can be established in two ways. In the conventional approach [11] the minimum-bias distribution on  $n_{ch}$  is partitioned by *standard bin edges* corresponding to centrality bins on the fractional cross section. The Glauber minimum-bias distributions are similarly partitioned. Mean values  $\langle n_{part} \rangle$ ,  $\langle n_{bin} \rangle$ ,  $\langle b \rangle$  and  $\langle n_{ch} \rangle$  are then obtained for each centrality bin. Alternatively, in the power-law context data and Glauber parameters can be related by *running integrals* (App. A 4), of which the binning method is a piece-wise special case. As with the binning method, the fractional cross section  $\sigma(n_{ch})/\sigma_0$  derived from data and the fractional cross section  $\sigma(b)/\sigma_{tot}$  from the Monte Carlo Glauber provide the contact between Glauber model and data.

As an example, we consider an analysis of 130 GeV RHIC data in which ten centrality classes were defined on multiplicity  $n_{ch} = n_{h+} + n_{h-}$  in one unit of pseudorapidity [12]. The raw  $dN_{evt}/dn_{ch}$  distribution was corrected for significant trigger and vertex-finding inefficiencies below  $n_{ch} = 50$  as follows. The raw data were scaled to agree with *Hijing* in the trusted  $n_{ch}$  interval [50,100] (as opposed to the [5,25] interval in [10]) where the collision dynamics were said to be dominated by A-A geometry and well-described by the *Hijing* model (the cited basis was [10], which however does not demonstrate the assumed behavior). The trigger/vertex efficiency below  $n_{ch} = 50$  was determined by the ratio of data to *Hijing* minimum-bias distributions, and the data were corrected by that ratio. That procedure gave a reported

overall trigger/vertex efficiency of 94%, with a 60% efficiency below  $n_{ch} = 5$ . The corrected distribution was normalized to 6.9 barns total cross section at 130 GeV as given by *Hijing* and partitioned by nine bin edges into ten bins according to the integrated fractional cross sections. It was reported in [12] that beam-gas and photonuclear contributions to the most-peripheral 20% bin were 30%. That bin was therefore excluded from further analysis.

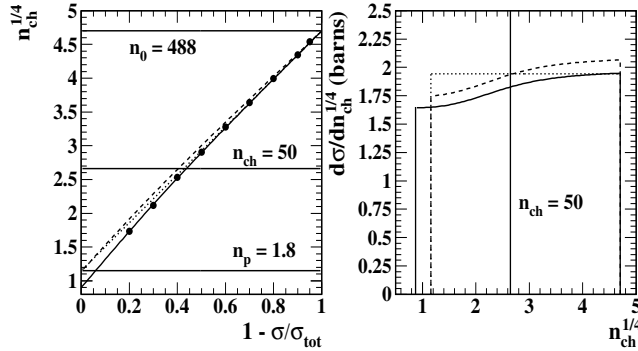


FIG. 7: Left panel: The points are bin edges from a conventional centrality definition [12]. The solid curve is a parameterization representing the points. The dashed curve is the solid curve with an adjusted fractional cross section. The dotted line is the power-law reference defined by the inferred  $n_p$  and  $n_0$  (see text). Right panel: The corresponding power-law forms of the differential cross section inferred from data (solid), with adjusted fractional cross section (dashed) and power-law reference (dotted) in the left panel.

In Fig. 7 (left panel) the points represent the ‘standard’ fractional cross-section bin edges on uncorrected  $n_{ch}$  in  $|\eta| < 0.5$  from Table I of [12]. We infer upper endpoint  $n_0 = 488$  by extrapolating the bin-edge positions with the power-law reference (dotted line);  $n_p = 1.8$  is the expected 130 GeV p-p yield into unit pseudorapidity acceptance: 2.25 [14] times the 80% TPC tracking efficiency. The edge positions for more-central collisions match the power-law reference precisely. An increasing deviation is observed for more-peripheral collisions. The solid curve is a simple parameterization representing the bin edges which can be used to reconstruct the differential cross section, shown as the solid curve in the right panel (with  $\sigma_{tot} = 6.9$  barns). The dotted lines in the right panel represent the power-law reference, corresponding to 6.9 barns distributed uniformly between the limiting multiplicities  $n_p$  and  $n_0$  noted above. The chosen normalization and fall-off in the data cross section for more peripheral collisions implies that the distribution must extend down to  $n_{ch} \sim 0.5$  ( $< 1/3$  the expected  $n_p$  value) to make up the total cross section. The cross-section displacement from the reference for peripheral collisions is 7%, corresponding to a nearly 100% systematic error in  $n_{part}$  (Sec. IX B).

The discrepancy can be removed by renormalizing the differential cross section in the right panel, or equivalently by adjusting the fractional cross section in the left panel so that the data trend extrapolates to the expected

$n_p$ . In the left panel  $\sigma/\sigma_0$  has been increased by 6% to produce the dashed curves in left and right panels. The criterion was extrapolation to  $n_p$  in the left panel. The physical content of the data distribution is otherwise retained. Such a correction is an example of an extrapolation constraint. The shape of this reconstructed minimum-bias distribution for 130 GeV data [12] seems inconsistent with that in Fig. 3 (right panel), also for 130 GeV data [10]. It is qualitatively inconsistent with the *Hijing* result in Fig. 2 (left panel).

## VIII. POWER-LAW CENTRALITY

The power-law approach to centrality determination is based on a running integral of the power-law differential cross-section distribution. That procedure removes the restriction to fixed centrality bins and a special  $n_{ch}$  definition. The general features of the result are represented by the cartoon in Fig. 8 (left panel). In an ideal case the running integral is well approximated by a straight line running from  $n_p^{1/4}$  to  $n_0^{1/4}$  on the vertical  $n_{ch}^{1/4}$  scale and from 0 to 1 on fractional cross section  $1 - \sigma/\sigma_0$ . The three parameters  $n_p$ ,  $n_0$  and the slope at the midpoint of the differential cross section largely define the shape of the running integral, the last parameter determining the curvature of the integral at its midpoint. Different curves in this left panel correspond to the range of slopes in Fig. 2 (right panel). The upper solid curve (data) can be compared with the dashed curve in Fig. 7 (left panel).

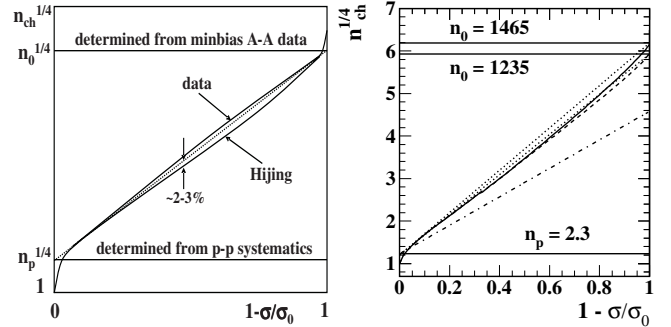


FIG. 8: Left panel: A cartoon of a running integral of the power-law differential cross section showing the principal features. Right panel: Running integrals of differential cross sections in Fig. 2 (left panel) for quench-off (dashed) and quench-on (solid) *Hijing*. The dotted lines drawn between  $n_p^{1/4}$  and  $n_0^{1/4}$  for each case are power-law references. The dash-dot line represents participant scaling. Note the coincidence of the *Hijing* curves and power-law reference below 0.2.

Fig. 8 (right panel) shows integrals of the *Hijing* differential power-law distributions in Fig. 2 (left panel). Integration substantially reduces statistical noise. Deviations from the straight-line power-law hypothesis (dotted lines) should consist mainly of a small curvature in the central region corresponding to the average slope of the differen-

tial power-law distribution, and small excursions near the endpoints corresponding to multiplicity fluctuations in p-p and central ( $b = 0$ ) Au-Au collisions. The curvatures for these *Hijing* data are concave upward, corresponding to the negative slope of the differential distribution in Fig. 2 (left panel). The dash-dot line is  $n_p^{1/4} \cdot (n_{part}/2)^{1/4}$  representing participant scaling (particle production independent of binary collisions).

The principal error sources for A-A centrality determination are said to be vertex reconstruction inefficiency and backgrounds (photonuclear and beam-gas) which might produce systematic deviations of tens of percent for peripheral collisions. The power-law approach provides two remedies: the data are brought into direct visual comparison with a simple reference to detect systematic effects, and the power-law trend itself provides a reliable extrapolation to p-p collisions if peripheral data cannot be corrected with confidence.

As argued in [10, 12], peripheral A-A collisions are expected to tend asymptotically to linear superpositions of N-N collisions, providing a basis to extrapolate trusted regions of the minimum-bias distribution into the peripheral region to reduce systematic error. It is *equivalent* to state that the differential minimum-bias distribution and its running integral should tend asymptotically to a power-law reference, which is essentially a folding of the p-p multiplicity distribution with the nearly-exact power-law  $n_{part}$  distribution. In [10, 12] extrapolations were made using the *Hijing* Monte Carlo. In Fig. 8 (right panel) the *Hijing* running integrals for peripheral collisions indeed converge to their power-law reference line before descending to 1 along the fluctuation detail. However, the use of *Hijing* for extrapolations can introduce significant systematic error, as we shall see below.

For more-central collisions non-trivial physical processes may cause legitimate deviations from the power-law reference, whereas *systematic-error* distortions of the distribution are expected to be small. For more-peripheral collisions, where systematic distortions may be large, physics-related deviations from N-N superposition should be small. The power-law reference thus provides a precise check of systematic corrections or an extrapolation in the event of severe systematic distortions. Concerns about residual systematic errors in cross-section measurements for peripheral collisions [10, 12] may have resulted from visual inaccessibility of the peripheral 20% bin within the conventional procedure. The resulting large uncertainty has typically led to abandonment of that important 20% region, whereas the power-law reference and extrapolation constraints may ironically provide the most accurate centrality measurement for the peripheral bin.

## IX. CENTRALITY ERROR

The three tasks of centrality determination previously defined each encounter systematic errors and uncertain-

ties. After correction there remain uncorrected systematic errors and associated uncertainties. The residual errors, different for conventional and power-law methods and for peripheral and central collisions, are reviewed in this section. We distinguish systematic errors for Glauber parameters and for data, and for the conventional method and the power-law method. In addition to absolute errors there are contributions from uncertainty in the *relative* centralities of Glauber model and data which affect particle production studies. Thus, common-mode reduction of systematic error is of interest.

### A. Total cross-section error

The nucleus-nucleus total cross section for Au-Au collisions can be estimated as follows. The Woods-Saxon matter distribution for Au has radius  $r_0 = 6.5$  fm (including an estimated 0.1 fm from the neutron ‘skin’) and diffuseness  $a = 0.5$  fm [11], giving a nominal nuclear edge at 7.5 fm. The nucleus-nucleus cross section is then  $\pi(2 \cdot 7.5 \text{ fm})^2 = 7.05$  barns. An uncertainty of 0.1 fm in the edge radius results in an uncertainty of 0.2 barns in the total cross section. That  $\pm 3\%$  range encompasses all Glauber results for RHIC Au-Au collisions. Knowledge of the physical total cross section  $\sigma_{tot}$  is not essential for centrality tasks 1) and 2). What we do require is the correct relation of data and Glauber to *fractional* cross section  $\sigma/\sigma_0$ .

### B. Glauber errors

The systematic errors for Glauber calculations and data are greatest for peripheral collisions. The optical Glauber can be ruled out on that basis, since peripheral values for  $n_{part}/2$  and  $n_{bin}$  by definition go to zero with  $1 - \sigma/\sigma_0$ , whereas the limiting case for physical collisions is 1 for both parameters. That observation is consistent with the results in Fig. 6 (right panels). The Monte Carlo Glauber on the other hand produces the correct asymptotic values, although there are quantitative systematic issues with integration methods, as discussed below.

To relate Glauber geometry parameters to data we connect the fractional cross-section dependencies in the two cases. The error propagation from fractional cross-section uncertainties to Glauber parameters is simply derived from the power-law parameterizations obtained above. For  $n_{part}$  we have  $\delta n_{part}/n_{part} = 4(3.72 - 1)\delta\sigma/\sigma_0$ , the coefficient being 10.9. For  $n_{bin}$  we have  $\delta n_{bin}/n_{bin} = 6(3.23 - 1)\delta\sigma/\sigma_0$ , the coefficient being 13.4. Both coefficients are large, and imply the need for tight control on the fractional cross section at the 1% level for effective geometry determination. In the power-law context that control is achieved by invoking an *extrapolation constraint*: *both parameters should extrapolate to 1 in the limit of N-N collisions or  $\sigma/\sigma_{tot} = 1$* .

Although systematic errors on  $n_{part}/2$  and  $n_{bin}$  for peripheral collisions are difficult to control without a constraint, those for path-length measure  $\nu$  are more tractable. We have  $\delta\nu/\nu = \{6 \cdot 2.23/n_{bin}^{1/6} - 4 \cdot 2.72/(n_{part}/2)^{1/4}\}\delta\sigma/\sigma_0$  with limiting values of the coefficient 2.5 (peripheral) and 1.25 (central). Thus, the error in  $\nu$  relative to the fractional cross section is  $O(1)$  whereas the relative errors in  $n_{part}/2$  and  $n_{bin}$  are  $O(10)$ . That result is a manifestation of *common-mode suppression* of systematic errors in the relative cross section due to the ratio structure of  $\nu$ .  $\nu$  is, in terms of systematic error at least, much superior to  $n_{part}$  as a centrality measure.  $\nu$  has the additional advantage that physical processes associated with initial-state parton scattering are, by hypothesis and observation, nearly linear on  $\nu$ , providing another precise visual reference.

### C. Data errors

In the absence of trigger/vertex inefficiencies the undistorted minimum-bias distribution would integrate to the total cross section corresponding to the intended trigger condition. Event loss due to trigger or vertex-reconstruction inefficiency results in distortion of the minimum-bias distribution and systematic error in the fractional cross section, which in turn leads to systematic error in the inferred collision geometry. In the conventional method of centrality determination the systematic uncertainty is greatest for peripheral collisions. The situation is illustrated in Fig. 9. Trigger/vertex inefficiencies, typically localized to peripheral collisions, as illustrated in the left panel, lead to uncertainty in the local distribution shape for peripheral collisions and uncertainty in the total cross section applied to the measured distribution.

In the conventional method the observed minimum-bias distribution is integrated from the central end downward to obtain the relation between  $n_{ch}$  and fractional cross section  $\sigma/\sigma_{tot}$ . Fig. 9 (right panel) shows that systematic error accumulates from central to peripheral collisions, and may become comparable to or exceed the centrality bin width for peripheral collisions, making centrality definition there impossible. That result contributes to abandoning the 20% most peripheral part of the cross-section range, which contains critical information on the transition from p-p to A-A collisions.

The conventional procedure does not make use of critical *a priori* information available from p-p collisions which can provide a precise constraint on the form of the minimum-bias distribution where it is most needed. Without such an *extrapolation constraint* the fractional cross section error can be 5-10% for peripheral collisions, making the  $n_{part}$  and  $n_{bin}$  parameters meaningless in that region. Attempts to provide an extrapolation for peripheral collisions using the *Hijing* Monte Carlo, as described in [10, 12], follows the spirit of an extrapolation constraint. However, we observe that *Hijing* is not a good model for peripheral A-A collisions, since it does not de-

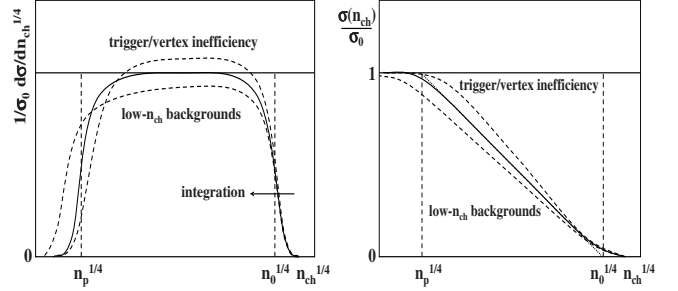


FIG. 9: Left panel: A cartoon of the power-law differential cross section for the ideal case (solid) and for two types of systematic error contribution (dashed). Right panel: A cartoon of the corresponding running integrals with resulting systematic errors, most prominent at the peripheral end.

scribe p-p collisions correctly.

Systematic errors and uncertainties for the power-law method are illustrated in Fig. 10. In the left panel the overall event efficiency (trigger plus vertex finding) is assumed to be uniform and high, except for peripheral collisions where the efficiency may fall considerably, possibly by multiples of 10%. The upper endpoint  $n_0$  is precisely known (< 2%) from the power-law minimum-bias distribution (but not the conventional method). The lower endpoint  $n_p$ , corresponding to the uncorrected p-p yield into the acceptance, can be inferred from separate experiments. The combination of those two numbers provides a precise extrapolation reference for the power-law relation between  $n_{ch}$  and  $\sigma/\sigma_{tot}$  as illustrated in Fig. 10 (right panel) .

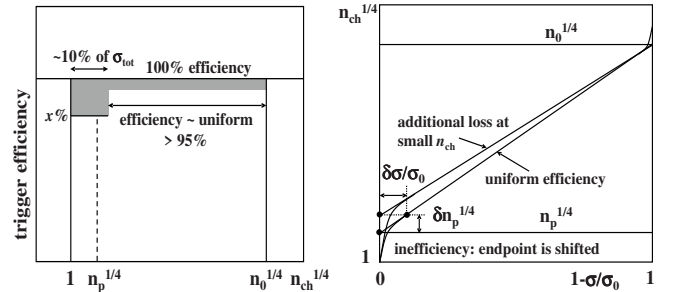


FIG. 10: Left panel: A cartoon of the power-law differential cross section illustrating typical trigger/vertex inefficiencies. Right panel: A cartoon of running integrals illustrating systematic errors resulting from inefficiencies in the left panel.

Inefficiency localized to peripheral collisions causes uncertainty in the fractional cross section. Assuming an error in the fractional cross section of 1%, what is the corresponding relative error of the extrapolated  $n_p^{1/4}$ ? We obtain  $\delta n_p/n_p = 4\delta n_p^{1/4}/n_p^{1/4} = 4(n_0^{1/4}/n_p^{1/4} - 1)\delta\sigma/\sigma_0$ . For Au-Au at 200 GeV in two units of pseudorapidity we have  $\delta n_p/n_p \simeq 4((1050/4)^{1/4} - 1) \times 1\% = 12\%$ , an unfavorable error propagation. However, if one knows the p-p multiplicity to about 10% one can limit systematic

error in the fractional cross section for data to 1% for peripheral collisions, a form of extrapolation constraint.

#### D. Error summary

The power-law context provides important control of systematic error for peripheral collisions, both for Glauber parameters and for the minimum-bias data distribution. Information derived from independent p-p measurements can be incorporated into the centrality problem as a constraint. The power-law method thus provides a *10-fold improvement* in centrality accuracy for peripheral collisions, making that critical region accessible for the first time. If the minimum-bias distribution is badly distorted over all centralities by experimental problems, the power-law form of the minimum-bias distribution provides a *fall-back determination* of collision centrality with useful accuracy. In general, propagation of error strongly favors the power-law strategy over the conventional method.

### X. PARTICLE PRODUCTION

In the context of the two-component model of nuclear collisions [15] it is of interest to determine what fraction of particle production in A-A collisions is due to participant scaling  $n_{ch} \propto n_{part}$  (soft component) and what fraction is due to binary-collision scaling  $n_{ch} \propto n_{bin}$  (hard component). Measurement of particle production in the form  $2/n_{part} \cdot n_{ch}$  is a stringent test of centrality determination, since the relation of  $n_{ch}$  to  $n_{part}$  is quite sensitive to small errors in fractional cross section  $\sigma/\sigma_0$  inferred separately in data and Glauber contexts. Without extrapolation constraints particle production trends are typically inaccessible for peripheral collisions due to excessive systematic error. Improvements in centrality accuracy are therefore especially important for particle-production studies.

In the power-law method  $n_{part}$ ,  $n_{bin}$  and  $\nu$  are represented by simple parameterizations on fractional cross section, which for centrality determination are sufficiently accurate. However, because the relevant parameter for particle production is  $n_{part}/2$  and not  $(n_{part}/2)^{1/4}$ , the sinusoid in Fig. 5 (upper-left panel)  $0.05 \sin\{2.6(n_{part}^{1/4} - 2.3)\}$  (relative to the mean power-law amplitude) plays a significant role and should be incorporated in the parameterization of  $n_{part}^{1/4}$  vs  $\sigma/\sigma_{tot}$ . The relative amplitude of the sinusoid on  $d\sigma/dn_{part}^{1/4}$  is 0.05. Therefore, the maximum deviation of  $\sigma(n_{part}^{1/4})/\sigma_{tot}$  from a power-law trend is 0.014 at the midpoint, which corresponds to a *relative* deviation of about 6% for  $n_{part}/2$  from its power-law trend, sufficient to warrant including the sinusoid in particle-production studies.

Fig. 11 (left panel) shows a cartoon of  $2/n_{part} \cdot n_{ch}$  vs

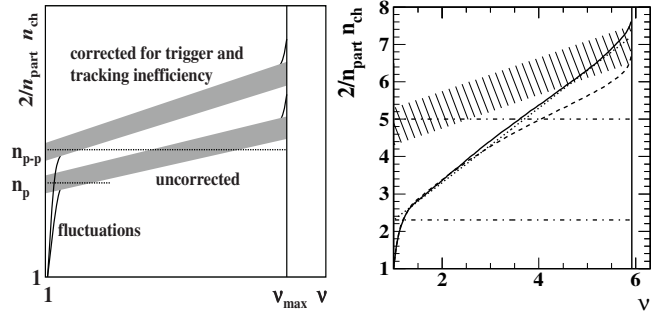


FIG. 11: Left panel: A cartoon of particle production per participant pair *vs* mean participant path-length  $\nu$  for uncorrected (lower) and corrected (upper) data. The effects of multiplicity fluctuations are illustrated at the ends. Right panel: Particle production curves for Hijing quench-off (dashed) and quench-on (solid) events. The dotted line represents a power-law reference. Results for RHIC data at 130 and 200 GeV are represented by the hatched band. The dash-dot lines represent the corrected p-p multiplicity in the acceptance at 200 GeV. The difference between Hijing and data is notable.

mean participant path length  $\nu$ . This plot combines  $n_{ch}^{1/4}$  *vs*  $1 - \sigma/\sigma_{tot}$  obtained from the data minimum-bias distribution and  $n_{part}^{1/4}$  and  $\nu$  *vs*  $1 - \sigma/\sigma_{tot}$  obtained from the Glauber Monte Carlo. The lower band represents uncorrected data, the upper band represents data corrected for tracking inefficiencies.  $n_p$  is the expected uncorrected p-p multiplicity in the acceptance, and  $n_{p-p}$  is the corrected value. The horizontal line extending to  $\nu_{max}$  corresponds to so-called ‘participant scaling,’ a limiting case of particle production. At each end, curves represent expected deviations from a power-law straight-line trend due to fluctuations.

Fig. 11 (right panel) shows the result of a particle-production study of the Hijing Monte Carlo, with  $n_{part}(b)/2$  *vs*  $\sigma(b)$  derived from the Glauber model in Fig. 5 (right panels) and  $n_{ch}$  *vs*  $\sigma(n_{ch})$  derived from curves in Fig. 8 (right panel). The quantity plotted is  $2/n_{part} \Delta\eta dn_{ch}/d\eta$ , with  $\Delta\eta = 2$ . The curves correspond to quench-off (lower, dashed) and quench-on (upper, solid) Hijing. The hatched region summarizes two-component trends observed for corrected RHIC data at 130 and 200 GeV [16], consistent with SPPS p- $\bar{p}$  data ( $\nu = 1$ ) at 200 GeV [17]. The dash-dot line corresponds to participant scaling from the expected  $dn_{ch}/d\eta = 2.5$  for p-p collisions at 200 GeV integrated over two units of pseudorapidity.

Quench-on (default) Hijing increases approximately linearly with  $\nu$ , whereas quench-off Hijing follows a curved trend. The difference, presumably due to added particle production resulting from jet quenching according to the pQCD Hijing model, is approximately quadratic in path length. The quadratic dependence may result from parton scattering ( $\propto \nu$ ) combined with jet quenching ( $\propto$  in-medium parton path length  $\sim \nu$ ). Fluctuation contributions appear more prominently in this plotting format as upturns or downturns at the ends of

the curves. Fluctuation amplitudes depend directly on detector acceptance and tracking efficiency, which thus may have substantial impact on minimum-bias distribution shapes measured with small detector acceptance and/or low tracking efficiency.

A striking feature of Fig. 11 (right panel) is the large discrepancy ( $\sim 2 \times$ ) between *Hijing* and *RHIC* data for peripheral collisions (dash-dot lines). That difference is especially surprising since *Hijing* is built on *Pythia* [18] as a standard representation of p-p collisions. It means that the *Hijing* minimum-bias distribution extends to substantially lower  $n_{ch}$  than data (below the observed  $n_p$ ), making it *inappropriate as an extrapolation* for minimum-bias data distributions. The apparent mismatch between data and assumed total cross section in Fig. 3 (right panel) and inferred large trigger inefficiencies for small multiplicities obtained using *Hijing* [10, 12] may also be explained by this feature.

## XI. TRANSVERSE MOMENTUM AND ENERGY PRODUCTION

Just as for charged-particle multiplicity, the production of transverse momentum  $p_t$  and energy  $E_t$  is determined partly by initial-state parton scattering and partly during the hadronization process. Thus,  $p_t$  and  $E_t$  production also exhibit a combination of participant scaling and binary-collision scaling. The analysis is similar to that for particle production and can also be illustrated with the *Hijing* Monte Carlo and *RHIC* data. These minimum-bias distributions are on continuous variables rather than the integers, requiring some differences in analysis details.

### A. *Hijing* $p_t$ data

We first construct a minimum-bias power-law distribution for  $p_t$  production. As a continuous measure,  $p_t^{1/4}$  was binned for this analysis into 50 equal bins, providing adequate resolution for peripheral edge structure. Event numbers were then accumulated directly into the bins on  $p_t^{1/4}$  (not  $p_t$ ). That procedure contrasts with the power-law distribution on multiplicity in Fig. 2 (left panel), where the conventional minimum-bias distribution was first formed on integer multiplicity  $n_{ch}$ , then rebinned onto  $n_{ch}^{1/4}$ . Fig. 12 (left panel) shows  $1/\sigma_0 d\sigma/dp_t^{1/4}$  vs  $p_t^{1/4}$ . The points on the left edge illustrate the bin spacing and edge resolution. As for  $n_{ch}$ , the upper half-maximum point  $p_{t0}$  estimates the correspondence on total  $p_t$  of  $b = 0$  and  $n_{part,max}$ , the lower half-maximum point  $p_{tp}$  estimates the average uncorrected total  $p_t$  in the acceptance for p-p collisions. The endpoints are  $p_{tp} \sim 0.8$  GeV/c and  $p_{t0} \sim 600$  (700) GeV/c for quench-off (quench-on) events respectively.

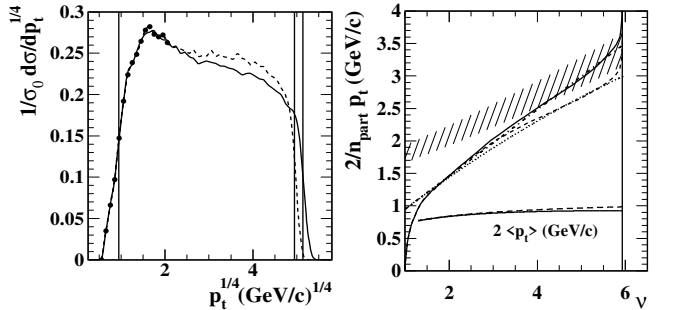


FIG. 12: Left panel: The power-law form of the minimum-bias distribution on total  $p_t$  within  $|\eta| < 1$  for quench-on (solid) and quench-off (dashed) *Hijing*. The points at left illustrate the uniform binning scheme. Right panel: The total  $p_t$  per-participant pair within the acceptance *vs* mean participant path length  $\nu$  for the two *Hijing* classes. The lower curves represent twice the *per-final-state-particle* mean  $p_t$   $2 \langle p_t \rangle$  for the two cases. The hatched region represents *RHIC* data for 130 and 200 GeV.

In Fig. 12 (right panel) we plot the total *per-participant-pair* quantity

$$2/n_{part} \Delta\eta dp_t/d\eta \equiv 2/n_{part} \Delta\eta dn_{ch}/d\eta \cdot \langle p_t \rangle, \quad (2)$$

with acceptance  $\Delta\eta = 2$ . The hatched region summarizes experimental trends for *RHIC* data at 130 and 200 GeV [16] consistent with 200 GeV p- $\bar{p}$  results ( $\nu = 1$ ) [17]. A related comparison has been made for transverse energy  $E_t$  [19] relevant to the next section. The *per-participant* total  $p_t$  plotted in the right panel exhibits a two-component trend (participant plus binary-collision scaling), with  $p_t$  produced *prior* to final-state hadronization scaling with the number of binary collisions. The nearly flat *Hijing*  $\langle p_t \rangle$  distributions in Fig. 12 (right panel) are consistent with our observation that particle production in *Hijing* increases with centrality at nearly the same rate as total- $p_t$  production.  $p_t$  production in central Au-Au collisions is predominantly from initial-state parton scattering *according to this model*.

The unique particle production systematics observed for *Hijing* collisions also impact *Hijing*  $\langle p_t \rangle$  *fluctuations* and related  $p_t$  *correlations* representing minijet structure in that model, as demonstrated in our previous *Hijing* studies [20, 21]. The centrality dependence of quench-on *Hijing* per-particle  $\langle p_t \rangle$  fluctuations was found to be approximately constant with centrality [20], strongly disagreeing with *RHIC* fluctuation measurements reported in [1]. We conclude that *Hijing* particle production has too large a binary-collisions or hard-scattering component (increases too rapidly with path length) compared to *RHIC* data, as indicated by Fig. 12 (right panel), and an anomalously low  $n_p$ , making it unsuitable for extrapolation purposes.

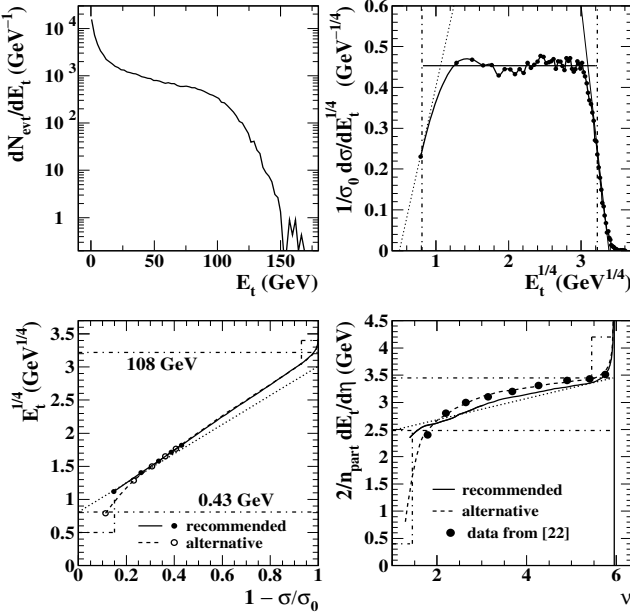


FIG. 13: Upper-left panel: The conventional semi-log form of the minimum-bias density distribution on total  $E_t$  in an EM-Cal patch (see text). Upper-right panel: The power-law form of the normalized minimum-bias density distribution on  $E_t$  for data from [22]. Lower-left panel: Running integrals of the distribution in the upper-right panel for two integral definitions (solid, dashed), compared to reference  $0.81(n_{part}/2)^{1/4}$  (dotted). Lower-right panel:  $E_t$  density on  $\eta$  per participant pair, comparing two running integrals of the data in the upper-right panel (solid and dashed) with an independent bin-based determination of  $E_t$  production from [22] (points).

## B. RHIC $E_t$ data

Fig. 13 (upper-left panel) shows a semi-log minimum-bias distribution on  $E_t$  deposited in an electromagnetic calorimeter (EMCal) [22]. The energy  $E_t$  deposited in a partial cylinder installed for these measurements (EMCal patch) was corrected to one unit of pseudorapidity and full azimuth for the lower-right panel by applying a factor 6. The  $E_t$  distribution was binned with uniform widths (2.34 GeV) on  $E_t$  except for the lowest bin (1.56 GeV). The  $E_t$  binning was apparently truncated at the low end by 0.78 GeV. Bin entries (event numbers)  $N_{evt,i}$  were converted for this analysis to densities  $dN_{evt,i}/dE_t$ , dividing by corresponding bin widths  $\delta E_{ti}$  to obtain the distribution in the upper-left panel.

In the upper-right panel the minimum-bias differential cross-section distribution is plotted in the power-law format. That distribution was multiplied bin-wise by Jacobian  $4E_{ti}^{3/4}$  and unit normalized to produce the upper-right plot. The half-maximum points  $E_{tp}^{1/4}$  and  $E_{to}^{1/4}$  are 0.81 (estimated) and 3.22  $\text{GeV}^{1/4}$  respectively. The thin diagonal lines at the ends represent on the right and estimate (dotted) on the left the fluctuation slopes. Comparison with the horizontal reference line shows that the

tribution is almost exactly power-law in form over the observed  $E_t$  interval. This distribution suffers from sparse sampling at the low- $E_t$  end, a critical region for centrality and production studies, and excessive sampling at the upper end. Uniform binning on  $E_t^{1/4}$  (and similarly for any continuous quantity) is strongly recommended, as illustrated by the  $p_t$  analysis of *Hijing* in Fig. 12 (left panel). The half-maximum points in the upper-right panel are represented in the lower-left and -right panels by horizontal dash-dot lines. The dash-dot boxes at lower left and right define the regions within which deviations from the power-law trend from fluctuations are expected, corresponding to the sloped end regions in the upper-right panel.

The lower-left panel shows two running integrals of the minimum-bias distribution in the upper-right panel. The solid curve and points represent the *recommended* running integral described in App. A 4. The dashed curve and open circles represent an *alternative* running-integral scheme in which 1) the bin widths on  $E_t$  are used to weight the bin contents  $N_{evt}$  of the original minimum-bias distribution (*not* densities  $dN_{evt}/dE_t$ ) and 2) the  $E_t$  values representing positions of running-integration limits are shifted down by 1.17 GeV,  $1/2$  the width of the uniform bins on  $E_t$ . The diagonal dotted line  $0.81 n_{part}^{1/4}$  is a participant-scaling reference.

The lower-right panel shows  $dE_t/d\eta$  per participant pair, with line styles as in the lower-left panel. A factor 6 was applied to  $E_t$  values to obtain  $dE_t/d\eta$  values according to the definition of the EMCal patch acceptance in [22]. The lower horizontal dash-dot line corresponds to the participant-scaling reference (dotted line) in the lower-left panel. The recommended form of running integral (solid line) follows the power-law reference (dotted diagonal line) closely, with small  $\sim 0.1$  GeV deviations corresponding to the actual structure of the differential minimum-bias density distribution at upper right. The solid points represent analysis results from [22]. The systematic error bars in that paper ( $\sim 0.5$  GeV) are omitted here, since the same underlying minimum-bias data are being used to compare different integration schemes. The points from [22] deviate significantly and systematically from the power-law reference and the recommended running integral. The dashed curve from the alternative integration scheme passes closely through the points, suggesting that the alternative scheme described in App. A 6 may have been used in that analysis.

In general, there is a dramatic difference between the shapes of the differential cross-section and per-participant  $E_t$  distributions in the right panels of Fig. 13 and the *Hijing*  $p_t$  data in Fig. 12, in contrast to a conclusion about the similarity of data and *Hijing* in [22]. Comparing these results to RHIC data for  $n_{ch}$  per participant, as summarized in Fig. 11 (right panel), suggests that  $E_t$  per particle may be constant or actually *decreasing* from peripheral to central collisions (from  $\sim 0.95$  to  $\sim 0.85$  GeV).

## XII. DISCUSSION

To unravel contributions to the final-state momentum distribution from parton scattering, subsequent in-medium dissipation, parton fragmentation and bulk-medium dynamics and fragmentation requires precise knowledge of collision geometry, including participant and binary-collision numbers, nucleus overlap geometry and mean participant path length, in relation to a physical observable, most commonly the particle multiplicity in a fiducial acceptance. We have compared the effectiveness of the conventional and power-law methods in analyzing Glauber model simulations and data to provide those relations.

The power-law method of centrality determination is substantially different from the conventional method in several ways. The method yields the following advantages: 1) it provides precise visual access to the entire minimum-bias distribution, 2) it provides a precise definition of endpoints  $n_p$  and  $n_0$  on the data minimum-bias distribution which have exact correspondence with the endpoints of the  $n_{part}$  distribution and the impact parameter, 3) it permits simple *linear* representations of the centrality dependence of Glauber parameters, 4) it permits simple extrapolations, or even *entire replacement*, of the experimental minimum-bias distribution when systematic errors cannot be corrected with confidence, 5) it permits flexible definition of centrality binning on  $n_{ch}$ , and 6) it provides the means to apply *a priori* extrapolation constraints which improve accuracy for peripheral collisions by  $10\times$  or more. Those advantages provide reliable access to the most peripheral 20% of collision centrality for the first time.

## XIII. SUMMARY

We have introduced a new technique for determining heavy ion collision centrality based on an observed power-law trend of the form  $n_{ch}^{-3/4}$  in the conventional minimum-bias distribution on particle multiplicity  $n_{ch}$ . That trend implies that transformation to a distribution on  $n_{ch}^{1/4}$  (power-law format) should confine *physics-related* variation to a limited range, which we have confirmed, permitting precise visual examination of distribution structure. The endpoints (half-maximum points) of the minimum-bias multiplicity distribution plotted in a power-law format correspond precisely to the endpoints of the participant-nucleon distribution, providing strong constraints on Glauber simulations used to connect collision geometry to particle multiplicity. We have determined that the power-law plotting format is applicable to Glauber  $n_{bin}$  and  $n_{part}$  minimum-bias distributions as well as  $n_{ch}$ ,  $p_t$  and  $E_t$ . The minimum-bias distribution on  $n_{part}$  is almost exactly of power-law form  $\propto n_{part}^{-3/4}$ , explaining the similar trend in data, and the distribution on  $n_{bin}$  is nearly  $\propto n_{bin}^{-5/6}$ , indicating that the distribution

on  $n_{bin}^{1/6}$  should be nearly constant, which we also confirm. The power-law minimum-bias distributions and associated techniques provide major improvement in the accuracy of centrality determination and precise access to variation with centrality of particle,  $p_t$  and  $E_t$  production in heavy ion collisions, which we have demonstrated with specific examples.

This work was supported in part by the Office of Science of the U.S. DoE under grant DE-FG03-97ER41020.

## APPENDIX A: BINNING AND RUNNING INTEGRATION

### 1. Binning

Confusion may arise if histogram bin entries are not well defined as to type. A bin entry may represent the *integral* of a density over the bin, or may estimate a *density* at the bin center obtained by dividing a bin integral by a bin width. The axes of a plot should consistently show either bin entries and bin centers or running-integral sums and corresponding *running-integral limits* (whether bin centers, edges or otherwise). When transforming a *density* from space  $x$  to space  $y$ , differential ratio  $dx/dy$  (Jacobian) relates the densities. However, discrete running integrals require appropriate *finite differences*, not differentials  $dx$  or  $dy$ .

### 2. Power-law transformation

The histogram bin entries for a raw minimum-bias distribution are event counts  $N_i$ , where  $i$  may be a bin index on continuous variable  $x$  such as  $p_t$  or  $E_t$ , or may be particle multiplicity  $n_{ch}$ .  $N$  is not in general a differential quantity. On a continuous space  $x$  it is the integral of a number density over a bin on  $x$ . If (possibly nonuniform) bin widths  $\delta x_i$  are defined on  $x$ , the minimum-bias *density* distribution is estimated by  $dN_i/dx \equiv N_i/\delta x_i$ . The power-law form is obtained by transforming densities by  $dN/dx^{1/4} \equiv 4x^{3/4}dN/dx$ .

For the power-law distribution on multiplicity,  $dN/dn_{ch}^{1/4} \equiv 4n_{ch}^{3/4}dN/dn_{ch} = 4n_{ch}^{3/4}N_{n_{ch}}$ . Assuming the ideal case (no trigger/vertex inefficiency), with  $N_{tot} \equiv \sum_i N_{n_{ch}}$ , we have  $1/\sigma_{tot} d\sigma/dn_{ch} \equiv 1/N_{tot} \cdot N_{n_{ch}}$ , with the power-law form of the differential cross section obtained as above. The transformation from conventional to power-law format is a non-linear map of one density distribution to another. The conventional minimum-bias distribution is a very non-uniform distribution on a uniform binning system. The power-law form is a nearly-uniform distribution on a non-uniform binning system. The latter makes the density and integration problem more accessible. However, proper integration must give *consistent* results in the two spaces.

### 3. Rebinning

In transforming a histogrammed density distribution from space  $x$  to space  $y$  rebinning may be desirable. As an example of a rebinning algorithm consider a density distribution  $f_n$  (e.g., event number) on integer variable  $x_n = n$ . We want a binned distribution  $g_k$  on some  $y$  interval with uniform bin widths  $\delta y$ , and with  $y_n = x_n^{1/4}$  and  $g_n = 4n^{3/4} f_n$ . We define uniformly-spaced bin edges  $\hat{y}_k$  on  $y$  with index  $k$ . We step through  $n$  and histogram elements  $g_n$ . Starting with bin  $k = 1$  on  $y$  we sum histogram elements  $g_n$  into  $G_k$ , number of steps on  $n$  within this  $k^{th}$  bin into  $M_k$ , and values  $n$  into  $N_k$  (this could also be values  $n^{1/4}$ ). We test the bin edge: if  $n^{1/4} < \hat{y}_k$  we continue the  $n$  loop. If not, we go to  $k + 1$  and continue the  $n$  loop. We increment  $k$  until the end of the specified  $y$  interval. We then form  $G_k/M_k = \bar{g}_k$  and  $N_k/M_k = \bar{n}_k$  (this could also be  $\overline{n^{1/4}}_k$ ) as uniformly-spaced transformed densities  $g_k$  and means  $\bar{n}_k^{1/4}$  (or  $\overline{n^{1/4}}_k$ ) on bin centers  $y_k = \hat{y}_k - \delta y/2$ . The minimum-bias distribution on particle multiplicity is thus rebinned to a ‘power-law’ distribution, as in Fig. 2 (left panel).

### 4. Running integrals

Numerical integration involves subtle issues with substantial impact. Systematic effects can be especially important for small index values (e.g., peripheral heavy ion collisions). Intuitive large-number approximations associated with continuous integration fail there, and integration methods must be reconsidered in detail. In plotting a running integral *vs* position each plotted running-integral value should be associated with the corresponding *running integration limit*, which may be a bin center or edge depending on the integral definition. In a nonlinear transformation from space  $x$  to space  $y$  the bin edges may no longer be symmetric about the point transformed from the original bin center, to a degree which depends on  $y$ . Some modification of the end weightings  $\alpha, \omega$  from 1/2 (see below) may be required. Finally, as a test of any adopted method, it should not matter in which direction the running integration is performed. We consider the definition of discrete integrals on discrete and continuous spaces, and examples from Glauber modeling and analysis of  $E_t$  production in heavy ion collisions.

The integration problem relevant to the Glauber model is running integrals on the space of integers. Integration on a discrete space can be defined by considering the additivity and symmetry properties of discrete integrals. Suppose  $f_n$  are histogram entries on integers  $n$  ( $f_n$  is then both density estimator and ‘integral’ over unit bin width). The integral additivity condition  $\sum_{n_1}^{n_2} f_n + \sum_{n_2}^{n_3} f_n = \sum_{n_1}^{n_3} f_n$  implies the discrete-integral definition on the interval  $[n_1, n_2]$   $\sum_{n_1}^{n_2} f_n \equiv \alpha f_{n_1} + f_{n_1+1} + \dots + f_{n_2-1} + \omega f_{n_2}$ , with  $\alpha + \omega = 1$ . If we require that bin edges be symmetric about integer

positions then  $\alpha = \omega = 1/2$ . Those conditions define the running integral on integers.

Discrete integrals on a continuous space have some features analogous to the discrete space. If  $f_i$  are densities at positions  $x_i$  on continuous variable  $x$ , and  $\delta x_i$  are (possibly varying) bin widths, the discrete total integral on interval  $[x_a, x_b]$  is  $F_{ab} = \sum_{i=a}^b f_i \delta x_i \equiv 1/2 f_a \delta x_a + f_{a+1} \delta x_{a+1} + \dots + f_{b-1} \delta x_{b-1} + 1/2 f_b \delta x_b$ . The discrete *running* integral is  $F_{am} = \sum_{i=a}^m f_i \delta x_i \equiv 1/2 f_a \delta x_a + f_{a+1} \delta x_{a+1} + \dots + f_{m-1} \delta x_{m-1} + 1/2 f_m \delta x_m$ . The corresponding running integration limits, increasing from endpoint  $x_a$ , are  $x_m = x_a + 1/2 \delta x_a + \delta x_{a+1} + \dots + \delta x_{m-1} + 1/2 \delta x_m$ . This assumes bins are symmetrically placed about bin centers  $x_i$ , and integration is between points  $x_i$ , not between leading and/or trailing bin edges. The choice depends on context and should be specified.

### 5. Integration and the Monte Carlo Glauber

We now consider the running integral in the Glauber context. Referring to Fig. 5 (right panels), the dotted lines in all cases represent power-law references. Taking as an example the upper-right panel, the solid curve represents the recommended running integral plotted *vs* corresponding running integration limit on the space  $n_{ch}^{1/4}$ , as described in this Appendix. The dash-dot curve, barely visible under the solid curve in the inset, represents an equivalent running integral on the space  $n_{ch}$  suitably transformed to  $n_{ch}^{1/4}$  which confirms the consistency of the definitions. Both curves accurately reflect the structure of the power-law differential distribution in the left panel in every detail, falling below and then recovering the dotted reference in the first two steps in accord with the initial excursion in the differential cross section, followed by a small sinusoidal deviation above the reference thereafter. Similar results are obtained in the lower-right panel. In particular, the solid and dash-dot curves there initially rise above the reference in response to the reduced initial values of the differential distribution, and then return asymptotically to the reference for more-central collisions.

In contrast, the solid points representing Glauber results from [12] deviate substantially from the power-law reference for more-peripheral collisions. We suspect that the source of the deviation is the definition of the integral used in [12]. To confirm this we constructed an alternative integral definition. The dashed curves (and open circles derived from individual points in the raw minimum-bias distributions) were obtained by the integral definition  $\sum_{n_1}^{n_2} f_n$  as above but with  $\alpha = \omega = 1$ ; that is, a *non-additive* integral definition. For that integral the first integration step contributes *twice as much* to the integral of  $1 - \sigma/\sigma_0$ , producing the substantial offset of the first step apparent in the insets of Fig. 5 (right panels). The limiting values of the ordinates (*effective* integration limits) apparent in the insets are then

bin edges at  $n_{part,p}^{1/4} = [(2 - 1.2 \cdot 0.5)/2]^{1/4} = 0.915$  and  $n_{bin,p}^{1/6} = [1 - 0.8 \cdot 0.5]^{1/4} = 0.918$ , not 1 as expected for physical collisions (the factors 1.2 and 0.8 correspond to the values of the differential distributions at their left endpoints). Aside from the initial offsets, the dashed curves do follow the details of the power-law differential distributions (run parallel to the solid curves) as they should. In resolving this integration issue the power-law format has reduced a troublesome 30% systematic *error* (for  $n_{part}/2$ ) to a small systematic *uncertainty*.

## 6. Integration and a RHIC $E_t$ analysis

Deviations of the  $E_t$  data (solid points) [22] from the recommended integral (solid) and power-law reference (dotted) in Fig. 13 (lower-right panel) suggest two binning/integration issues: 1) An extra bin-width factor may have been added to the running integral of the minimum-bias distribution. For minimum-bias bin entries  $N_{evt,i}$  (integral quantities, not densities) the unit-normal running integral should be  $1/N_{tot} \sum_{i=1}^m N_{evt,i}$  (with  $\alpha = \omega = 1/2$ , as noted above). The alternative running integral may have been of the form  $\sum_{i=1}^m N_{evt,i} \delta E_{ti} / \sum_{i=1}^M N_{evt,i} \delta E_{ti}$ , including as weights bin widths  $\delta E_{ti}$ , uniform except for the left-most bin which is narrower and produces the problem. Because of the narrow first bin, inclusion of the extra factor would

shift the apparent power-law trend in Fig. 13 (lower-left panel) to smaller values of  $1 - \sigma/\sigma_0$  for given  $E_t^{1/4}$ , producing a left-shift of points increasing for more-peripheral collisions. The running integral must converge by construction to the limit  $1 - \sigma/\sigma_0 = 1$  at  $E_{tot} = 108$  GeV for central collisions, fixing that end of the curve. Including the bin widths would therefore cause significant *elevation* of the data trend from [22] *above* the recommended integral (solid curve and points) in the lower-left panel for more-peripheral collisions.

2) The corresponding  $E_t$  values may have been shifted down by  $1/2$   $E_t$  bin or 1.17 GeV. Such a shift would produce a down-shift of points in Fig. 13 (lower-left panel), increasing nonlinearly for more-peripheral collisions with distorting consequences for the  $E_t$  production plot at lower right. Combining the two assumptions to define an *alternative* running integral we obtain the dashed curves in the lower two panels, with open circles corresponding to specific entries in the minimum-bias distribution at upper right. In the lower-right panel the resulting dashed curve passes quite close to all the data points from [22]. The alternative ‘running integral’  $\sum_{i=1}^m \delta E_{ti} \cdot N_i$  is improper in that  $N_i$  is already an integral quantity, including implicitly a bin-width factor (*i.e.*,  $N_i = \delta E_{ti} \cdot dN_i/dE_t$ ). While the dashed curve appears to describe the [22] data trend well, those data do not necessarily result from the above integration scheme.

---

[1] J. Adams *et al.* (STAR Collaboration), Phys. Rev. C **71** 064906 (2005), (nucl-ex/0308033).

[2] J. Adams *et al.* (STAR Collaboration), submitted to Phys. Lett. B (2005), nucl-ph/0406035.

[3] J. Adams *et al.* (STAR Collaboration), submitted to Phys. Lett. B (2005), nucl-ph/0411003.

[4] T. A. Trainor and D. J. Prindle (STAR Collaboration), hep-ph/0506177, to appear in the proceedings of the MIT Workshop on Correlations and Fluctuations in Relativistic Nuclear Collisions, Cambridge, Massachusetts, 21-23 Apr 2005.

[5] R. Jefferson Porter and Thomas A. Trainor (STAR Collaboration), hep-ph/0506172, to appear in the proceedings of the MIT Workshop on Correlations and Fluctuations in Relativistic Nuclear Collisions, Cambridge, Massachusetts, 21-23 Apr 2005.

[6] D. H. Hardtke, Department of Physics, University of California - Berkeley, private communication.

[7] M. Gyulassy and X. N. Wang, Comp. Phys. Comm. **83** (1994) 307; X. N. Wang and M. Gyulassy, Phys. Rev. D 44 (1991) 3501.

[8] A. J. Baltz, C. Chasman and S. N. White, Nucl. Instrum. Meth. A **417**, 1 (1998)

[9] J. Gonzalez (STAR Collaboration) Department of Physics, University of California - Los Angeles, private communication.

[10] C. Adler *et al.* (STAR Collaboration), Phys. Rev. Lett. **87**, 112303 (2001)

[11] M. Miller, Department of Physics, Yale University, Ph.D. Thesis, December, 2003 (unpublished).

[12] J. Adams *et al.* (STAR Collaboration), submitted to Phys. Rev. C (2003), nucl-ph/0311017.

[13] W. Busza *et al.*, Phys. Rev. Lett. **34**, 836 (1975).

[14] F. Abe *et al.*, Phys. Rev. D **41**, 2330 (1990)

[15] D. Kharzeev and M. Nardi, Phys. Lett. B **507**, 121 (2001).

[16] B. B. Back *et al.*, (Phobos Collaboration), Phys. Rev. Lett. **89**, 22302 (2002); A. Bazilevski *et al.*, (Phenix Collaboration), Nucl. Phys. **A715**, 486c (2003).

[17] C. Albajar *et al.* (UA1 Collaboration), Nucl. Phys. **B 335**, 261 (1990).

[18] Sjöstrand T 1994 Comput. Phys. Commun. **82** 74  
Sjöstrand T, Lönnblad L, Mrenna S and Skands P 2003, hep-ph/0308153.

[19] V. Topor Pop *et al.*, Phys. Rev. C **68**, 054902 (2003), nucl-th/0209089.

[20] Q. J. Liu and T. A. Trainor, Phys. Lett. B **567**, 184 (2003).

[21] Q. J. Liu, D. J. Prindle and T. A. Trainor, accepted to Phys. Lett. B (2005), hep-ph/0410180.

[22] J. Adams, *et al.*, (STAR Collaboration) Phys. Rev. C **70**, 054907 (2004).